PHYSICAL REVIEW B **106**, 205106 (2022)

Root-N Krylov-space correction vectors for spectral functions with the density matrix renormalization group

A. Nocera[1] and G. Alvarez[2]

[1]*Department of Physics and Astronomy, Stewart Blusson Quantum Matter Institute, University of British Columbia, Vancouver, BritishColumbia, Canada V6T, 1Z4*

[2]*Computational Sciences and Engineering Division, Oak Ridge National Laboratory, Oak Ridge, Tennessee 37831, USA*

(Received 20 April 2022; revised 26 September 2022; accepted 17 October 2022; published 3 November 2022)

We propose a method to compute spectral functions of generic Hamiltonians using the density matrix renormalization group (DMRG) algorithm directly in the frequency domain, based on a modified Krylov-space decomposition to compute the correction vectors. Our approach entails the calculation of the root-N ($N = 2$ is the standard square root) of the Hamiltonian propagator using Krylov-space decomposition and repeating this procedure N times to obtain the actual correction vector. We show that our method greatly alleviates the burden of keeping a large bond dimension at large target frequencies, a problem found with conventional correction-vector DMRG, whereas achieving better computational performance at large N. We apply our method to spin and charge spectral functions of t-J and Hubbard models in the challenging two-leg ladder geometry and provide evidence that the root-N approach reaches a much improved spectral resolution compared to the conventional correction vector.

DOI: 10.1103/PhysRevB.106.205106

I. INTRODUCTION

In condensed-matter physics, several unusual properties of strongly correlated quantum materials are unveiled using *spectroscopic* techniques, such as angle-resolved photoemission spectroscopy (ARPES) [1], inelastic neutron scattering (INS), and resonant inelastic x-ray scattering (RIXS) [2]. These experimental probes do not provide a direct access to the ground state but rather explore the low-energy excitations of the system. Excitation spectra are experimentally measured looking at the energy and momentum exchanged by the probe of each technique with the material: a photoemitted electron for ARPES, a neutron for INS, a photon for RIXS and are theoretically encoded in *spectral functions*. The progressive improvement in momentum and energy resolution in an experimental spectroscopic apparatus calls on the theory side for an equally significant improvement of the spectral functions calculations accuracy.

For a one-dimensional (1D) lattice Hamiltonian of size L, a generic spectral function can be defined as

$$O(q,\omega) = \frac{1}{L}\sum_{i,j} e^{iq(i-j)} \int_0^\infty dt\, e^{i(\omega+E_g)t} \langle\psi|\hat{O}_i e^{-i\hat{H}t}\hat{O}_j|\psi\rangle, \tag{1}$$

where $|\psi\rangle$ is the ground state of the system Hamiltonian $\hat{H}$, E_g is the ground-state energy, q and ω are the momentum and frequency (or energy) of the electron in the material, and $\hat{O}_j$ is the relevant operator involved in the scattering process of the specific technique acting locally on site "j" ($\hat{O}_j = \hat{c}_{j\sigma}$ for ARPES, $\hat{O}_j = \hat{S}^z_j$ for INS, whereas special care is needed for RIXS as written in Ref. [3]).

In 1D, the most powerful method to compute spectral functions of arbitrary strongly correlated Hamiltonians is the density matrix renormalization group (DMRG) [4,5]; the DMRG is a variational but systematically exact algorithm to find a matrix product state (MPS) representation for the ground state of the system [6]. Spectral functions can be computed in the time-space domain using time-dependent matrix product state methods [7–10]. (For a recent review of the different variants, see Ref. [11]) When using time evolution, the problem is to find an efficient MPS representation of the time-evolved vector,

$$|x_j(t)\rangle = e^{-i\hat{H}t}\hat{O}_j|\psi\rangle, \tag{2}$$

where the ground state of the Hamiltonian $\hat{H}$ is locally modified by $\hat{O}_j$, and the resulting state is evolved up to a very large (in principle, "infinite") time. This evolution always grows the entanglement of the state and, thus, spoils the compression of the MPS representation. Simulations are, therefore, typically stopped at some large or maximum time, and linear prediction [9] or recursion methods [12] are needed to obtain a well-behaved Fourier transform in frequency.

In this paper, we are concerned with the complementary approach of computing the spectral functions *directly in the frequency domain.* To discuss this case, it helps to rewrite the spectral function as

$$O(q,\omega) = \lim_{\eta\to 0}\frac{1}{L}\sum_{i,j} e^{iq(i-j)} \times -\frac{1}{\pi}\mathrm{Im}\left[\langle\psi|\hat{O}_i \frac{1}{\omega-\hat{H}+E_g+i\eta}\hat{O}_j|\psi\rangle\right], \tag{3}$$

2469-9950/2022/106(20)/205106(9)

where one writes down the Hamiltonian propagator explicitly, and $\eta > 0$ is an arbitrary small extrinsic spectral broadening. Three are the approaches that are typically used by DMRG practitioners. Historically, the hybrid DMRG-Lanczos-vector methods were first introduced [13] (refined using MPS more recently [14,15]), then afterwards the correction-vector (CV) method [16–21] and Chebyshev polynomial methods [22–25] were proposed. In the CV method, one computes the real and imaginary parts of the correction vector,

$$|x_j(\omega + i\eta)\rangle = \frac{1}{\omega - \hat{H} + E_g + i\eta}\hat{O}_j|\psi\rangle, \tag{4}$$

at fixed frequency ω, finite broadening η, and then computes the spectral function in real-frequency space as a standard overlap $\langle\psi|\hat{O}_i|x_j(\omega + i\eta)\rangle$. The real and imaginary parts of the correction vector are typically obtained by solving for coupled matrix equations using conjugate-gradient methods [16], or by minimizing a properly defined functional [18,19]. Reference [20] formulated the algorithm in MPS language.

In 2016, we proposed [21] an alternative method to compute directly the correction vectors using a Krylov-space expansion of the Hamiltonian operator constructed starting from the locally modified MPS $|\phi\rangle = \hat{O}_j|\psi\rangle$. In all these cases, the entanglement content of the correction vectors is large, and it can be very large for large frequencies. This makes standard CV DMRG simulations very expensive for Hamiltonians beyond spin systems or for large lattices.

In 2011, Holzner *et al.* [22] proposed a MPS method to compute a Chebyshev polynomial expansion (truncated at some order N) of the spectral function (CheMPS). In this approach, the Chebyshev momenta can be obtained from overlaps of a properly defined series of Chebyshev vectors. The main advantage of CheMPS lies in the small entanglement that each Chebyshev vector has because the method *redistributes* the large entanglement of the correction-vectors $|x_j(\omega + i\eta)\rangle$ for different frequencies (or, alternatively, the time-evolved state $|x_j(t)\rangle$) over the entire series of Chebyshev vectors.

Inspired by this idea, we here propose a method to compute a generalized correction vector with smaller entanglement content, the root-N correction vector, defined as

$$\left|x_j^{1/N}(\omega + i\eta)\right\rangle = \left(\frac{1}{\omega - \hat{H} + E_g + i\eta}\right)^{1/N}\hat{O}_j|\psi\rangle. \tag{5}$$

The idea is to construct the actual correction vector as the final vector of the series $\{|x_j^{p/N}(\omega + i\eta)\rangle\}_{p\in[1,N]}$ after N applications of the root-N propagator. At first sight, it seems that, if N is sufficiently large, constructing the entire series of vectors just adds a computational overhead compared to the standard DMRG CV algorithm because only the final vector of the series is actually needed for the spectral function calculation. Yet we will show that the entanglement content of the series slowly builds up with p, and, therefore, going through many intermediate steps is more efficient than the conventional DMRG CV algorithm, which tries to compute the last element of the series in one step only.

The paper is organized as follows. Section II A introduces the main steps of the algorithm; Sec. II B analyzes the algorithm's computational performance, and the entanglement content of the root-N correction vectors in the test case of a Heisenberg model in the two-leg ladder geometry. Section II C applies our root-N method to compute spin and charge spectral functions of doped t-J and Hubbard models in the challenging two-leg ladder geometry, showing how our method improves the spectral *resolution* and increases the signal-to-noise ratio at large frequencies. Finally, we present our conclusions and outlook.

II. METHOD AND RESULTS

A. root-N CV method algorithm

The algorithm follows five steps. We assume a standard DMRG approach but provide the main step of the algorithm in MPS language in the Appendix.

(1) Compute the ground-state wave function with the DMRG.

For each frequency ω, repeat steps 2–4 to cover the desired interval $[\omega_{\min}, \omega_{\max}]$ with some step $\Delta\omega > 0$:

(2) Apply operator O_j at the center of the chain and build the $p = 1$ root-N correction vector $|x_j^{p/N}(\omega + i\eta)\rangle$ as in Eq. (5). This can be performed using conventional DMRG as described in Ref. [21]. The Appendix describes in detail the algorithm in MPS language. In this stage, as in the conventional CV method, the sources of error are two: the Lanczos error in the tridiagonal decomposition of the Hamiltonian (or effective Hamiltonian in MPS language) indicated below by $\epsilon_{\text{Tridiag}}$; the SVD error of the multitargeting DMRG procedure (state averaging in MPS language).

Repeat step 3 until the Nth root-N correction vector is constructed and optimized, then go to step 4.

(3) Build the $p + 1$ root-N correction vector $|x_j^{(p+1)/N}(\omega + i\eta)\rangle$ from the previous one assuming it as a starting point for the Krylov-space decomposition of the Hamiltonian. A few DMRG sweeps are performed until a desired convergence is reached.

(4) Measure the spectral function in real-frequency space as the overlap $\langle\psi|\hat{O}_i|x_j(\omega + i\eta)\rangle$; this part is the same as in conventional DMRG CV.

(5) Fourier transform the overlap $\langle\psi|\hat{O}_i|x_j(\omega + i\eta)\rangle$ to get the dynamical structure factor in momentum space $O(\mathbf{q}, \omega) = \frac{1}{L}\sum_{i,j} e^{iq(i-j)}\langle\psi|\hat{O}_i|x_j(\omega + i\eta)\rangle$.

To clarify the main steps of the algorithm, we draw an analogy with the adaptive time-step targeting approach introduced for time-dependent DMRG in the seminal paper by Feiguin and White [26]. In this case, one constructs the time-evolved vector $|x_j(\delta t)\rangle = U(\delta t)\hat{O}_j|\psi\rangle$ only for *small* time-step intervals of length $\delta t = t/N$, and where $U(\delta t) = e^{-i\hat{H}\,\delta t}$ is the time-evolution propagator. To get the final time-evolved vector at time t, one repeatedly applies $U(\delta t)$ to the MPS. In practice one does not build the evolution operator $U(\delta t)$ in the local basis but rather directly constructs the vector $|x_j(\delta t)\rangle = U(\delta t)\hat{O}_j|\psi\rangle$ using a Krylov-space decomposition of the Hamiltonian (or effective Hamiltonian in MPS language).

In our proposed root-N Krylov-space approach, we introduce a propagator in a fictitious time-space s as $|x_j(\delta s)\rangle = W(\delta s)\hat{O}_j|\psi\rangle$, where $\delta s = 1/N$, and where $W(\delta s) = e^{-\hat{K}\,\delta s}$ with $\hat{K} = \ln[\omega + E_g + i\eta - \hat{H}]$. Clearly, if we apply $W(\delta s)N$

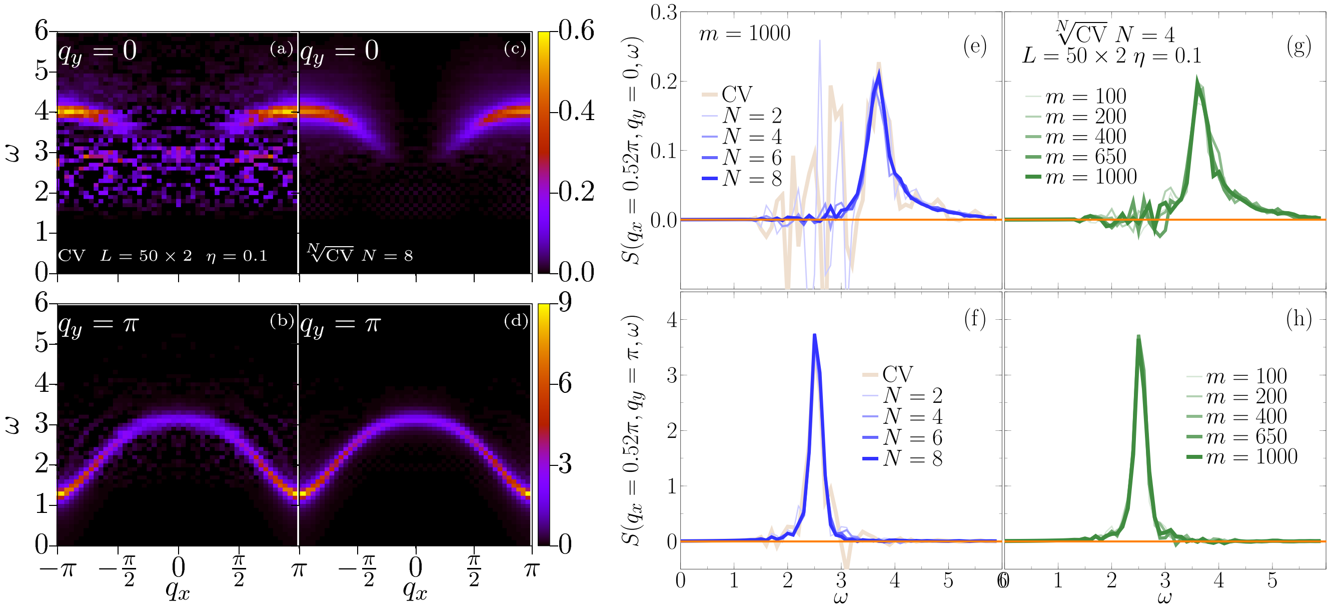

FIG. 1. Convergence analysis of the root-N Krylov-space CV DMRG method: the Heisenberg ladder. Panels (a) and (b) report the $q_y = 0, \pi$ components of $S(q_x, q_y, \omega)$ using the standard Krylov-space CV approach. A ladder with $J_y = 2J_x$ is simulated. The length is $L = 50 \times 2$, the broadening is $\eta = 0.1$, and the resolution step is $\delta\omega = 0.1$ (units are set by $J_x = 1$). Panels (c) and(d) report the $q_y = 0, \pi$ components of $S(q_x, q_y, \omega)$ using the root-N Krylov-space CV method using $N = 20$. Panels (e) and (f) show specific momentum-energy line cuts of the dynamical spin structure computed in panels (a)–(d) for different values of the *root-exponent* N. Numerical fluctuations and instabilities are removed, and the quality of the spectra is clearly improved as N is increased. Panels (g) and (h) show the same line cuts as in panels (e) and (f) but with at fixed N and increasing the number of DMRG states. When using the root-N CV method with $N = 4$, a substantially smaller number of states $m = 200$–$650 < 1000$ suffices to get better quality results than with the standard Krylov-space DMRG CV approach.

times to initial vector $\hat{O}_j|\psi\rangle$ we obtain the desired standard correction vector. In other words, we *formally* define and solve an auxiliary differential equation,

$$\frac{d}{ds}\left|x_j^s(\omega+i\eta)\right\rangle = -\ln\left[\omega+E_g+i\eta-\hat{H}\right]\left|x_j^s(\omega+i\eta)\right\rangle, \quad (6)$$

such that at time s we have the solution,

$$\left|x_j^s(\omega+i\eta)\right\rangle = \left(\frac{1}{\omega-\hat{H}+E_g+i\eta}\right)^s\left|x_j^0(\omega+i\eta)\right\rangle, \quad (7)$$

with the initial condition being $|x_j^0(\omega+i\eta)\rangle = \hat{O}_j|\psi\rangle$.

In this construction, $1/N$ plays the role of a *small* parameter to compute the resolvent in the standard CV approach. We will show that this method is especially useful at large target frequencies where large bond dimensions (or DMRG states) are typically needed.

B. Convergence analysis and computational performance: the Heisenberg model on a two-leg ladder as a case study

We begin by testing our root-N CV method by applying it to an isotropic Heisenberg model on a two-leg ladder geometry. (The Supplemental Material [27] provides computational details for all the models considered in this paper.) The Heisenberg Hamiltonian on a two-leg ladder with open boundary conditions and size $L = L_x \times 2$ is defined as

$$H_{\text{Heis}} = J_x \sum_{i=1;\,\gamma=1,2}^{L_x-1} \mathbf{S}_{i,\gamma}\cdot\mathbf{S}_{i+1,\gamma} + J_y\sum_{i=1}^{L_x}\mathbf{S}_{i,1}\cdot\mathbf{S}_{i,2}, \quad (8)$$

where $\mathbf{S}_{i,\gamma} \equiv \{S_{i,\gamma}^x, S_{i,\gamma}^y, S_{i,\gamma}^z\}$ describes the spin-(1/2) operators on site i and ladder leg γ. In this paper, antiferromagnetic exchange interactions along both the leg and the rung directions are assumed with $J_y = 2J_x$. The spin structure factor $S(\mathbf{q}, \omega)$ with $\mathbf{q} \equiv (q_x, q_y)$ can be defined as

$$S(\mathbf{q},\omega) = \frac{1}{2L_x}\sum_{j=1;\gamma}^{L_x} e^{i[q_x(j-i)+q_y(\gamma-\gamma')]} \times \langle\psi|\mathbf{S}_{j,\gamma}\frac{1}{\omega-H+i\eta}\mathbf{S}_{i,\gamma'}|\psi\rangle, \quad (9)$$

where the *center* point is chosen in the middle of leg 1, $(i, \gamma') = (L_x/2, 1)$.

Figures 1(a) and 1(b) report spectral maps of the two components $q_y = 0, \pi$ of the dynamical spin structure factor $S(\mathbf{q}, \omega)$ as a function of the momentum transfer q_x along the leg direction and of the frequency. These are obtained with conventional CV as in Refs. [21,28] on a system size of length $L = 50 \times 2$ and with an extrinsic broadening parameter $\eta = 0.1J_x$. By comparison, Figs. 1(c) and 1(d) reports results obtained using the root-N CV method with $N = 8$. In both cases, we have used a maximum $m = m_{\max} = 1000$ DMRG states and a minimum $m_{\min} = 200$, keeping the truncation error below 10^{-7}. Our DMRG calculations were carried out with the DMRG++ code [29]. [Please see the description around Eq. (A4) in the Appendix for the definition of the extended MPS which is optimized by SVD in the root-N CV algorithm.] We clearly note an overall improved spectrum in

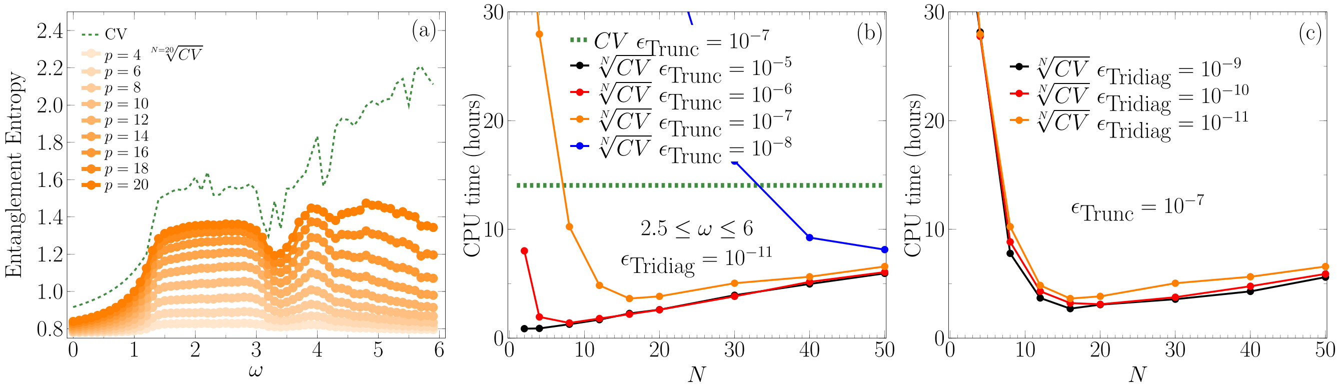

FIG. 2. Entanglement entropy of the root-N Krylov correction vectors and computational performance of the method. Panel (a) Entanglement entropy computed with conventional CV (dark green) compared to the same quantity computed with the root-N CV; $N = 20$ and different p values (indicated by orange lines and thickness increasing with p) as a function of ω. We have used a Heisenberg two-leg ladder with $J_y = 2J_x$, length $L = 50 \times 2$ as in Fig. 1. (b) Accumulated CPU time in hours (obtained summing all the CPU times of the CV simulations in the frequency interval $\omega \in [2.5, 6]$) for different values of the DMRG truncation error $\epsilon_{\rm Trunc}$ and (c) for different values of the Krylov-space threshold accuracy parameter $\epsilon_{\rm Tridiag}$ as a function of the *root-exponent* N. The simulations were run on a single Intel Xeon CPU E5-1620 CPU node. When compared with the standard Krylov-space correction-vector method, the performance of the root-N approach is superior for sufficiently large N.

this case with respect to the conventional CV method. We analyze below the spectral features in more detail.

Figures 1(e) and 1(f) show momentum $q_x = 0.52\pi$ line cuts of the spin spectra for the $q_y = 0, \pi$ components in the root-N CV method. The data show that by increasing the *root-exponent* N numerical fluctuations and instabilities are removed with respect to the conventional CV results. The red curves in Figs. 1(e) and 1(f) show that the conventional CV approach can yield negative values for certain frequencies. As finite-size effects are small for a $L = 50 \times 2$ ladder, these are clearly artifacts of the CV method which might spoil important properties of the spectral functions, such as sum rules. On the contrary, the root-N CV approach shows always positive values which progressively improve upon increasing the root-exponent N. Figures 1(g) and 1(h) show how well the root-N method converges with respect to the number of DMRG states. Contrary to panels (a)–(d), in these panels the data for $m < 1000$ were obtained by imposing the zero truncation error in the DMRG SVDs, therefore, setting $m = m_{\rm max} = m_{\rm min}$. Our data show that at fixed root-exponent $N = 4$, a substantially smaller number of DMRG states $m =$ 200–650 < 1000 is sufficient to get better quality results than with the conventional CV approach. As we will show next, this improvement can be understood by the much lower entanglement content of the root-N correction vectors.

Figure 2(a) shows indeed that the entanglement content of the root-N correction vectors is smaller than the actual (conventional) correction vector. In this calculation, to compute the entanglement entropy of the expanded MPS for root-N correction vectors (Appendix Eq. (A4) has the definition), we have used a maximum $m = 2000$ DMRG states (and a minimum $m_{\rm min} = 200$), keeping the truncation error below 10^{-8} in both methods. It is nice to see that the entanglement entropy of the extended MPS in the root-N CV method is very close to that of the conventional CV in the lower-frequency range investigated $\omega \in [0, \omega^*]$ with $\omega^* \simeq 4.5$. For larger frequencies, the root-N CV approach truncates the entanglement contained in the conventional CV vector, showing that a larger root-exponent N or a larger number of DMRG states should be considered. Yet we highlight that this truncation does not show instabilities or fluctuations as in the conventional CV approach.

In the same range of frequencies ($\omega \in [2.5, 6]$), we have monitored the accumulated CPU times taken for the simulations to complete in the two methods [Fig. 2(b)]. We observe that, for moderately small root-exponent N, the root-N CV method can be actually slower than the conventional CV method, assuming the same truncation error $\epsilon_{\rm Trunc}$ and truncation threshold $\epsilon_{\rm Tridiag}$ for the Hamiltonian matrix decomposition in the Krylov space (see Appendix for a more detailed definition of $\epsilon_{\rm Tridiag}$). If the root-exponent N is sufficiently large, the root-N CV method is seen to be computationally more efficient than the conventional CV method. Indeed, when the entanglement is decomposed in smaller chunks by considering a larger N, the root-N method becomes faster even though many more optimizations and Lanczos decompositions are actually performed. Eventually, however, if the root-exponent N is very big, the increased number of DMRG sweeps and iterations required to compute the larger number of root-N vectors becomes naturally detrimental for computational performance as the accumulated CPU times are seen to increase linearly with N.

Figure 2(b) further shows that at fixed root-exponent N as one decreases the requested DMRG truncation error $\epsilon_{\rm Trunc}$, the accumulated CPU times are bigger. This is because of the larger computational load of the SVD decomposition of the MPS tensors in the multitargeting or state-averaging approach.

Figure 2(c) ends this subsection by showing further how the accumulated CPU times vary as a function of the truncation thresold $\epsilon_{\rm Tridiag}$ for the Hamiltonian matrix decomposition in the Krylov space at fixed DMRG truncation error $\epsilon_{\rm Trunc}$. A smaller threshold requires a larger number of steps and, thus, a bigger Krylov space, requiring a larger CPU time to converge and complete the simulations.

C. Correlation functions of *t*-*J* and Hubbard models

In this section, we apply the root-*N* CV method to the more challenging *t*-*J* and Hubbard models on a two-leg ladder geometry.

The *t*-*J* Hamiltonian is defined as

$$
\begin{aligned}
H_{t\text{-}J} = &-t_x \sum_{i=1;\,\gamma=1,2;\sigma}^{L_x-1} (c^{\dagger}_{i,\gamma,\sigma} c_{i+1,\gamma,\sigma} + \text{H.c.}) \\
&- t_y \sum_{i=1;\sigma}^{L_x} (c^{\dagger}_{i,1,\sigma} c_{i,2,\sigma} + \text{H.c.}) \\
&+ J_x \sum_{i=1;\,\gamma=1,2}^{L_x-1} \left(\mathbf{S}_{i,\gamma} \cdot \mathbf{S}_{i+1,\gamma} - \frac{n_{i,\gamma} n_{i+1,\gamma}}{4} \right) \\
&+ J_y \sum_{i=1}^{L_x} \left(\mathbf{S}_{i,1} \cdot \mathbf{S}_{i,2} - \frac{n_{i,1} n_{i,2}}{4} \right),
\end{aligned}
\qquad (10)
$$

where $c^{\dagger}_{i,\gamma,\sigma}$ $(c_{i,\gamma,\sigma})$ is the electron creation (annihilation) operator on site i, ladder leg γ with spin polarization σ, whereas $n_{i,\gamma} = \sum_{\sigma} c^{\dagger}_{i,\gamma,\sigma} c_{i,\gamma,\sigma}$ is the electron number operator. The Hubbard Hamiltonian is

$$
\begin{aligned}
H_{\text{Hub}} = &-t_x \sum_{i=1;\,\gamma=1,2;\sigma}^{L_x-1} (c^{\dagger}_{i,\gamma,\sigma} c_{i+1,\gamma,\sigma} + \text{H.c.}) \\
&- t_y \sum_{i=1;\sigma}^{L_x} (c^{\dagger}_{i,1,\sigma} c_{i,2,\sigma} + \text{H.c.}) + U \sum_{i=1;\,\gamma=1,2}^{L_x} n_{i,\gamma,\uparrow} n_{i,\gamma,\downarrow}.
\end{aligned}
\qquad (11)
$$

For both models defined above, the spin structure factor $S(\mathbf{q}, \omega)$ is defined as in the Heisenberg model case [Eq. (9)]. Analogously, the charge structure factor is

$$
\begin{aligned}
N(\mathbf{q}, \omega) = &\frac{1}{2L_x} \sum_{j=1;\gamma}^{L_x} e^{i[q_x(j-i)+q_y(\gamma-\gamma')]} \\
&\times \langle \psi | \delta n_{j,\gamma} \frac{1}{\omega - H + i\eta} \delta n_{i,\gamma'} | \psi \rangle,
\end{aligned}
\qquad (12)
$$

where $\delta n_{j,\gamma} \equiv n_{j,\gamma} - \langle \psi | n_{j,\gamma} | \psi \rangle$, where $|\psi\rangle$ is the ground state of the system.

We start discussing the *t*-*J* model results, comparing the root-*N* method against the results obtained to the conventional CV approach. We calculate both spin and charge dynamical structure factors for a doped ladder with $N_{\text{el}} = 0.88L$, corresponding to 12% hole doping and with lattice size $L = 50 \times 2$. In this case, we use a maximum $m = 1200$ DMRG states for both methods (and a minimum $m_{\text{min}} = 200$) in order to keep the truncation error below 10^{-8}.

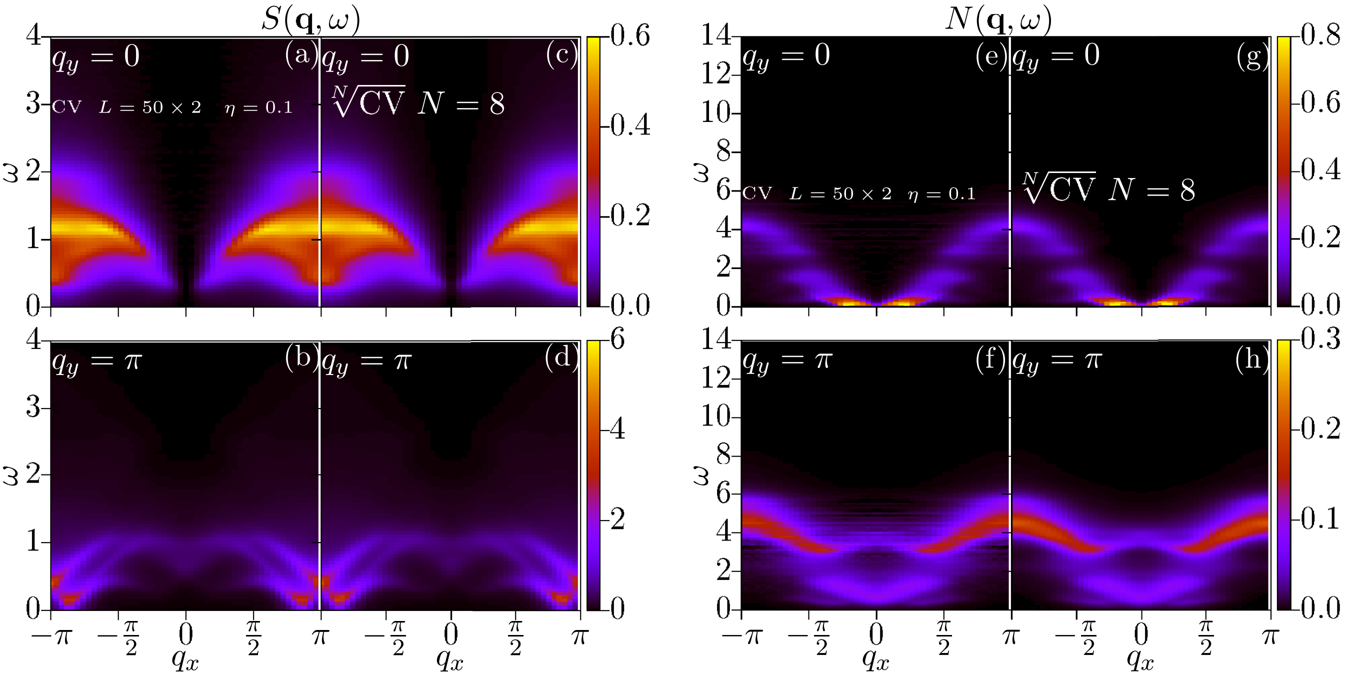

FIG. 3. Dynamical structure factors for a *t*-*J* two-leg ladder. Panels (a) and (b) [(e) and (f)] report the $q_y = 0, \pi$ components of the $S(q_x, q_y, \omega)$ $[N(q_x, q_y, \omega)]$ using the standard Krylov -pace correction-vector approach. A ladder with $t_y = t_x = t = 1$, $J_x = J_y = 0.5t$ is simulated. The length is $L = 50 \times 2$, the number of electrons is $N_{\text{el}} = 0.88L$, the broadening is $\eta = 0.1$, and the resolution step $\delta\omega = 0.1$ (units are set by $t = 1$). Panels (c) and (d) [(g) and (h)] report the $q_y = 0, \pi$ components of the $S(q_x, q_y, \omega)$ $[N(q_x, q_y, \omega)]$ using the root-*N* Krylov-space correction vector using $N = 8$.

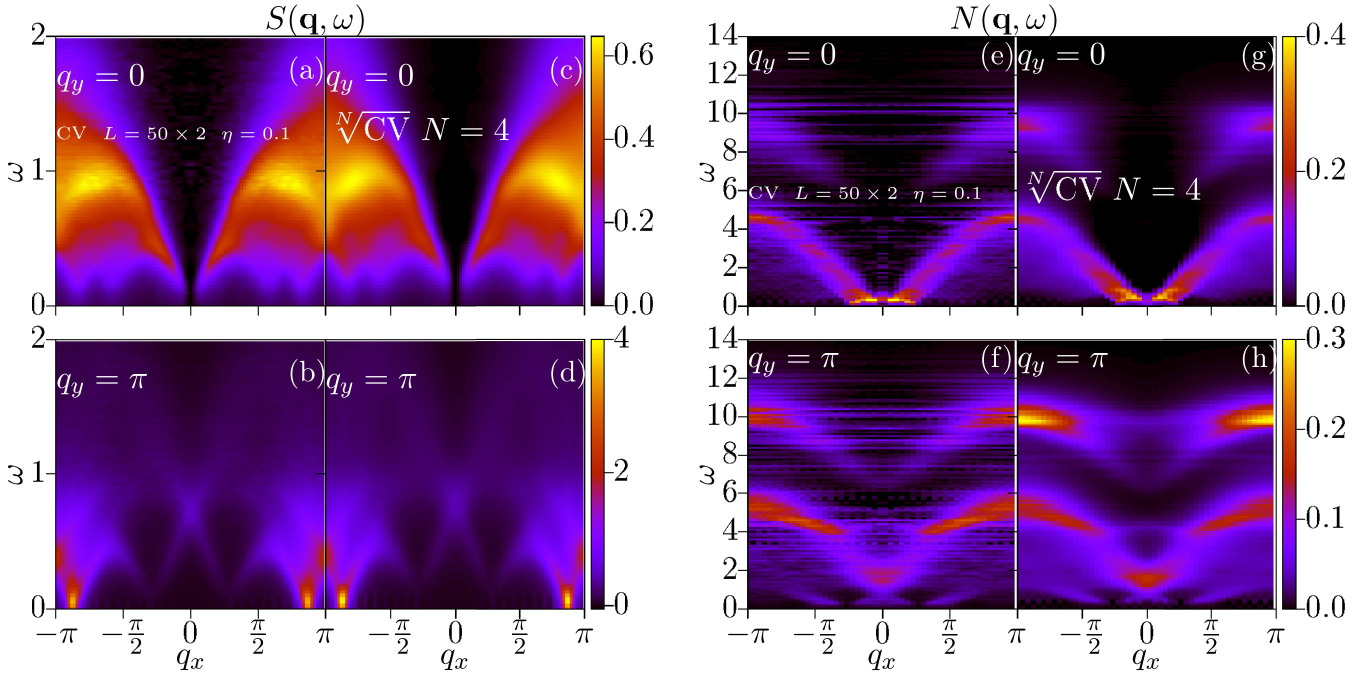

FIG. 4. Dynamical structure factors for a Hubbard two-leg ladder. The $q_y = 0$ and $q_y = \pi$ components of the dynamical spin structure factor $S(q_x, q_y, \omega)$ using in (a) and (b) the conventional Krylov-space DMRG CV approach, against in (c) and (d) the root-N Krylov-space CV method with $N = 4$ (a maximum of $m = 3000$ DMRG states were used). The $q_y = 0$ and $q_y = \pi$ components of the dynamical charge correlation using in (e) and (f) the conventional Krylov-space DMRG CV against in (g) and (h) the root-N Krylov-space CV with $N = 4$ (a maximum of $m = 2000$ DMRG states were used). A ladder $L = 50 \times 2$ ladder with $t_y = t_x = t = 1$, $U = 8t$ is simulated with $N_{\mathrm{el}} = 0.88L$ electrons, broadening $\eta = 0.1$, and resolution step $\delta\omega = 0.025$ for $S(q_x, q_y, \omega)$, and $\delta\omega = 0.1$ for $N(q_x, q_y, \omega)$. Units are set by $t = 1$.

Figures 3(a)–3(d) show the comparison for the dynamical spin structure factor $S(\mathbf{q}, \omega)$. We note that for $N = 8$ the root-N CV method yields results that are practically identical to those obtained with the CV method. Yet the root-N method provides a much better frequency resolution or larger signal-to-noise ratio for the more challenging dynamical charge structure factor $N(\mathbf{q}, \omega)$ where we also obtain quantitative agreement.

To summarize, the dynamical spin structure factor $S(\mathbf{q}, \omega)$ is practically identical in the two methods, whereas when considering the dynamical charge structure factor $N(\mathbf{q}, \omega)$ besides obtaining qualitative agreement, the root-N provides a much better frequency *resolution* (or a larger signal-to-noise ratio as we recall here that in both methods the same broadening η was used).

We now focus on the Hubbard model where minor differences in the results between the two methods can be observed when a moderately small root-exponent N is used in the root-N CV method.

As in the t-J case, we consider spin as well as charge dynamical structure factors for a doped ladder ($N_{\mathrm{el}} = 0.88L$, 12% hole doping) with system size $L = 50 \times 2$. We consider an isotropic ladder with parameters $t_x = t_y = t = 1$ and $U = 8t$. Spin and charge structure factors for Hubbard ladders were already studied and discussed by us in Refs. [30–34] where the conventional Krylov-space CV method was used. Figure 4 uses a maximum of $m = 3000$ DMRG states in both methods for $S(\mathbf{q}, \omega)$ whereas a maximum of $m = 2000$ was used for $N(\mathbf{q}, \omega)$. In both cases, the minimum number of DMRG states was $m_{\min} = 200$, and the truncation error was kept smaller than 10^{-7}.

Figures 4(a)–4(d) show the comparison for the dynamical spin structure factor $S(\mathbf{q}, \omega)$. For $N = 4$ the root-N CV method gives results practically identical to the CV method, and only minor quantitative differences can be observed. For example, in the root-N method, the broad two-triplon excitation band in the spin structure factor $S(q_x, q_y = 0, \omega)$ appears to be sharper than in the conventional CV method. In the $q_y = \pi$ component, instead, the main spectral features at the incommensurate wave-vector $q_x \simeq 0.88\pi$ appear slightly broader in the conventional CV method as a function of frequencyat low frequencies. From this analysis, we conclude that even a moderately small root-exponent N is sufficient to get a better converged spin spectral function using the root-N CV method.

These observations are relevant when comparing DMRG spectral data with RIXS [35] and INS [36] experiments in the challenging "telephone number" cuprates, experimental data that recently have became available for the doped regime [34].

Finally, we discuss the dynamical charge structure factor, which is of interest in RIXS measurements of the charge-transfer band excitations in ladder cuprates. When a Hubbard ladder is doped with holes with respect to half-filling, we observe two branches in the $N(\mathbf{q}, \omega)$: the first one at low energy corresponds to in-band particle-hole excitations across the Fermi level. The high-energy band describes charge-transfer electronic exitations above the Mott gap. Figures 4(e)–4(h) shows that the root-N CV method provides high quality spectral data with no appreciable shifts (downwards or upwards) of the main features. (Please remember that we are using the same η for both methods.) Yet some spectral weight redistribution can be noted: spectral intensity on the high-energy charge-transfer band appears more intense in the root-*N* CV method compared to the conventional CV method. We conclude that in this case, even though very good results can be obtained with a modest root-exponent *N*, one should prefer simulations with the largest possible *N* in order to get the best results from our root-*N* method.

III. DISCUSSIONS AND CONCLUSIONS

In this paper, we have proposed a method to compute generic spectral functions of strongly correlated Halmiltonians using generalized correction vectors with smaller entanglement content: the root-*N* CV method. The idea behind the root-*N* CV draws inspiration, in part, from time-dependent MPS methods, and, in part, from the Chebyshev MPS approach. The CheMPS method helps in computing spectral functions but as was highlighted recently [25], whereasresolving accurately the low-energy part of the spectral functions, CheMPS cannot resolve the high-energy spectrum accurately because an energy truncation of the Chebyshev vectors is, in general, required. To avoid this issue, Xie *et al.* [25] have proposed a reorthogonalization scheme for the Chebyshev vectors (ReCheMPS). Nevertheless, if the target frequency window for the spectral function is chosen to be much smaller than the many-body width of the system (this should be, in general, performed to increase the frequency resolution), an energy truncation might still be required. There is evidence that the energy-truncation procedure severely limits the applicability of the CheMPS or ReCheMPS methods in challenging cases as in Hubbard or t-J models as in these cases it likely becomes a necessary step of the algorithm mainly because the many-body bandwidth is, in general, much larger than the spectral support of typical spectral functions. When the energy truncation is performed, several Krylov-space projections as Chebyshev recurrence steps are required, rendering the method as computationally demanding as the conventional CV method.

Going back to the root-*N* CV, this paper has shown that when the root-exponent *N* is sufficiently large, the root-*N* CV performance becomes better than that of the conventional CV because the former method handles much less entangled correction vectors. In particular, we have shown evidence that in the Heisenberg and t-J models the root-*N* CV method improves even the quality of the spectral functions and provides a better frequency spectral resolution (or a larger signal-to-noise ratio). Larger *N* values in the root-*N* CV method require more sweeping of the lattice but do not affect much CPU times because each sweep is faster than using smaller *N* values.

Finally, the challenging Hubbard model requires a careful use of our root-*N* CV method: whereas moderately small root-exponents *N* give very good results for the main spectral features, our data show only minor differences with respect to the conventional CV method, which, however, should be taken into account when high-precision experimental results are available.

We believe that root-*N* correction-vector DMRG will become a much used method not only when high-precision spectral data is sought, but also when high performance is required, performance better than the computationally expensive conventional CV method.

The root-*N* method should also facilitate high-precision spectral function calculations in finite width cylinders where better computational methods are currently needed. These cylinders try to approach the two-dimensional models that are at the frontier of what DMRG can perform, and they need a very large computational effort to simulate.

ACKNOWLEDGMENTS

We thank P. Laurell and T. Barthel for discussions and for carefully reading the paper. A.N. acknowledges support from the Max Planck-UBC-UTokyo Center for Quantum Materials and Canada First Research Excellence Fund (CFREF) Quantum Materials, the Future Technologies Program of the Stewart Blusson Quantum Matter Institute (SBQMI), and the Natural Sciences and Engineering Research Council of Canada (NSERC). This work used computational resources and services provided by Compute Canada and Advanced Research Computing at the University of British Columbia. G.A. was partially supported by the Scientific Discovery through the Advanced Computing (SciDAC) Program funded by U.S. DOE, Office of Science, Advanced Scientific Computing Research and BES, Division of Materials Sciences and Engineering.

APPENDIX: MPS ALGORITHM TO BUILD THE ROOT-*N* CORRECTION VECTOR

Let us introduce a Matrix product state representing the ground state of the system for L sites and open boundary conditions (we use a notation similar to Ref. [11]),

$$|\psi\rangle = \sum_{\substack{\sigma_1\cdots\sigma_L\\ m_0\cdots m_L}} M^{\sigma_1}_{1;m_0,m_1}\cdots M^{\sigma_L}_{L;m_{L-1},m_L}|\sigma_1\cdots\sigma_L\rangle, \tag{A1}$$

where m_j are the bond dimensions or virtual indices (with m_0 and m_L one-dimensional dummy indices), and σ_j represent the physical indices of the many-body state of the system. Formally, let us define the tensors $\bar{\psi}_{L,j-1} \equiv (M_1^\dagger, \ldots, M_{j-1}^\dagger)$ and $\bar{\psi}_{R,j+1} \equiv (M_{j+1}^\dagger, \ldots, M_L^\dagger)$ which constitute a left and right map, respectively, from the joint Hilbert space on sites 1 through $j-1$ onto the bond space m_{j-1}, and from the joint Hilbert space on sites $j+1$ through L onto the bond space m_j. If we apply these maps to the MPS $|\psi\rangle$, we can obtain the effective state at site j, $|\psi_j^{\text{eff}}\rangle$; see Fig. 5(a). When $|\psi\rangle$ is in a MPS mixed-canonical form, $|\psi_j^{\text{eff}}\rangle$ equals the three-rank tensor $M_{j,m_{j-1}m_j}$ in the MPS at site j, which is often interpreted as a vector of dimensions $(d_j m_{j-1} m_j)$, where d_j is the local physical Hilbert space dimension. Similarly, the Hamiltonian $\hat{H}$, in matrix product operator form, acts between the maps defined above [and their conjugates, $\psi_{L,j-1}$ $\psi_{R,j+1}$; see Fig. 5(b)] to yield an effective single-site Hamiltonian $\hat{H}_j^{\text{eff}}$. This procedure can also be defined in the space of two sites. A computer program never needs to explicitly construct $\hat{H}_j^{\text{eff}}$, but only evaluates its action on $|\psi_j^{\text{eff}}\rangle$.

Using $|\psi_j^{\text{eff}}\rangle$ and $\hat{H}_j^{\text{eff}}$, we construct three local MPS tensors. The first one is obtained by applying operator $\hat{O}_j$ on

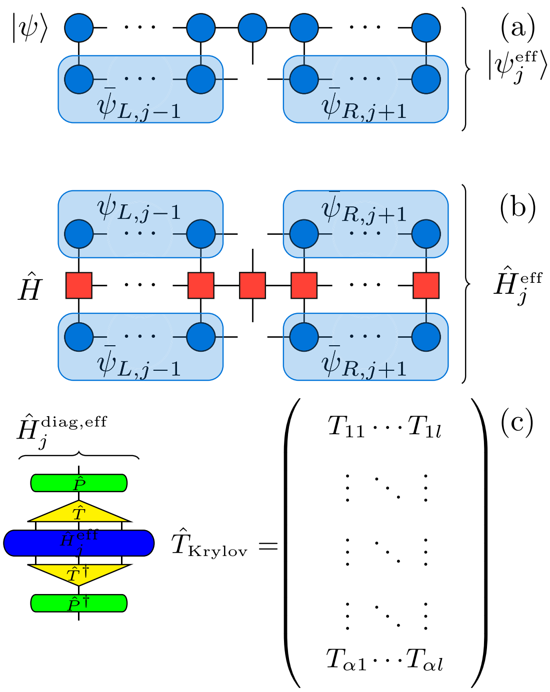

FIG. 5. Effective local state vector and Hamiltonian. Panel (a) Effective state $|\psi_j^{\mathrm{eff}}\rangle$ obtained by projecting the MPS by the maps $\bar{\psi}_{L,j-1} \equiv (M_1^\dagger, \ldots, M_{j-1}^\dagger)$ and $\bar{\psi}_{R,j+1} \equiv (M_{j+1}^\dagger, \ldots, M_L^\dagger)$. If $|\psi\rangle$ is a mixed-canonical MPS representation, then simply $|\psi_j^{\mathrm{eff}}\rangle = M_j$. Panel (b) Effective (one-site) Hamiltonian obtained by projecting $\hat{H}$ using the maps $\{\bar{\psi}_{L,j-1}, \psi_{L,j-1}, \bar{\psi}_{R,j+1}, \psi_{R,j+1}\}$ defined above. Analogous definitions can be given in the two-site case. Panel (c) (left) Graphical representation of the diagonal effective Hamiltonian projected onto the Kryrol space. Representation of the Krylov projection operator (triangular yellow tensor) $T_{l\alpha}$ where $\alpha = \{\sigma_j, m_{j-1}, m_j\}$ joins three indices so that it can be represented as a matrix (right). $\hat{T}$ tridiagonalizes $\hat{H}_j^{\mathrm{eff}}$ of panel (b), $\hat{H}_j^{\mathrm{Tridiag,eff}} = T^\dagger \hat{H}_j^{\mathrm{eff}} T$, to the smaller Krylov space spanned by index l, $\dim[l] \ll \dim[\alpha] = d_j \dim[m_{j-1}]\dim[m_j]$. P_{ln} (green tensor) diagonalizes $\hat{H}_j^{\mathrm{Tridiag,eff}}$.

$|\psi_j^{\mathrm{eff}}\rangle$, yielding $|\phi\rangle = \hat{O}_j|\psi\rangle$. The MPS $|\phi\rangle$ has all the tensors equal to those of $|\psi\rangle$ except for the one at site j, $M'_{j;m_{j-1},m_j}$,

$$M'^{\sigma_j}_{j;m_{j-1},m_j} = \sum_{\sigma'_j} O_j^{\sigma_j\sigma'_j} M^{\sigma'_j}_{j;m_{j-1},m_j}. \tag{A2}$$

We then construct the (real and imaginary parts of the) root-N correction vector by Krylov-space decomposition of the Hamiltonian $\hat{H}_j^{\mathrm{eff}}$,

$$\begin{aligned}[X(\omega + i\eta)]^{\sigma_j}_{j;m_{j-1},m_j} &= \sum_{\substack{l,l'nn'\\ \sigma'_j,m'_{j-1},m'_j}} T^\dagger_{l;\sigma_j,m_{j-1},m_j} P^\dagger_{ln} \frac{1}{[\omega - \epsilon_j^{\mathrm{eff}}\delta_{nn'} + E_g + i\eta]^{1/N}} \\ &\quad \times P_{n'l'} T_{l';\sigma'_j,m'_{j-1},m'_j} M'^{\sigma'_j}_{j;m'_{j-1},m'_j},\end{aligned} \tag{A3}$$

where $T_{l';\sigma_j,m_{j-1},m_j}$ tridiagonalizes $\hat{H}_j^{\mathrm{eff}}$, $\hat{H}_j^{\mathrm{Tridiag,eff}} = T^\dagger \hat{H}_j^{\mathrm{eff}} T$ to the smaller Krylov space spanned by index l, $\dim[l] \ll d_j \dim[m_{j-1}]\dim[m_j]$. P_{ln} diagonalizes $\hat{H}_j^{\mathrm{Tridiag,eff}}$, $\hat{H}_j^{\mathrm{diag,eff}} = P^\dagger \hat{H}_j^{\mathrm{Tridiag,eff}} P$, where $\epsilon_j^{\mathrm{eff}}$'s are the eigenvalues of $\hat{H}_j^{\mathrm{diag,eff}}$. How is the Krylov-space tridiagonalization of $\hat{H}_j^{\mathrm{eff}}$ stopped? In practice, we compare the lowest eigenvalue of $\hat{H}_j^{\mathrm{diag,eff}}$, $\epsilon_{\min} = \{\epsilon_j^{\mathrm{eff}}[k]\}_{\min}$ at iterations k and $k+1$, and exit the loop when the error breaks below a certain threshold. In this paper, we have set $\epsilon_{\mathrm{Tridiag}}$ to a value not too small in order to avoid the proliferation of Krylov vectors (and, thus, Lanczos iterations), and their reorthogonalizations. In general, the three states $|\phi\rangle$, $|X^{\mathrm{Re}}\rangle$, and $|X^{\mathrm{Im}}\rangle$ will be represented in a bad basis of the environments ψ_L and ψ_R which are optimized to represent original state $|\psi\rangle$. To expand these bases, we use state averaging of the four states, which is equivalent to targeting more than one state in conventional DMRG language. In MPS language as explained in Ref. [37], the state averaging is performed by creating an extra index which labels the states involved. One formally considers an expanded MPS representing a mixed state,

$$\begin{aligned}\begin{pmatrix}|\psi\rangle\\ |\phi\rangle\\ |X^{\mathrm{Re}}\rangle\\ |X^{\mathrm{Im}}\rangle\end{pmatrix} &= \sum_{\sigma_1\cdots\sigma_L} A_1^{\prime,\bar{\sigma}_1}\cdots C_j^{\prime,\bar{\sigma}_j}\cdots B_L^{\prime,\bar{\sigma}_L}|\sigma_1\cdots\sigma_L\rangle \\ &= \sum_{\sigma_1\cdots\sigma_L} \begin{pmatrix} A_1^{\sigma_1}[\psi] & 0 & 0 & 0\\ 0 & A_1^{\sigma_1}[\phi] & 0 & 0\\ 0 & 0 & A_1^{\sigma_1}[X^{\mathrm{Re}}] & 0\\ 0 & 0 & 0 & A_1^{\sigma_1}[X^{\mathrm{Im}}]\end{pmatrix} \\ &\quad \cdots \begin{pmatrix} C_j^{\sigma_j}[\psi]\\ C_j^{\sigma_j}[\phi]\\ C_j^{\sigma_j}[X^{\mathrm{Re}}]\\ C_j^{\sigma_j}[X^{\mathrm{Im}}]\end{pmatrix} \\ &\quad \cdots \begin{pmatrix} B_L^{\sigma_L}[\psi] & 0 & 0 & 0\\ 0 & B_L^{\sigma_L}[\phi] & 0 & 0\\ 0 & 0 & B_L^{\sigma_L}[X^{\mathrm{Re}}] & 0\\ 0 & 0 & 0 & B_L^{\sigma_L}[X^{\mathrm{Im}}]\end{pmatrix} \\ &\quad \times |\sigma_1\cdots\sigma_L\rangle,\end{aligned}$$

where $C^{\prime,\bar{\sigma}_j}_{j;m'_{j-1},m'_j}$ has four components (representing the four *targeted* vectors) and it has extended bond dimensions $m'_{j-1} = m_{j-1}^{[\psi]} + m_{j-1}^{[\phi]} + m_{j-1}^{[X^{\mathrm{Re}}]} + m_{j-1}^{[X^{\mathrm{Im}}]}$ and $m'_j = m_j^{[\psi]} + m_j^{[\phi]} + m_j^{[X^{\mathrm{Re}}]} + m_j^{[X^{\mathrm{Im}}]}$. Here, the notation in terms of A and B tensors underlines a mixed-canonical representation of all the MPSs. By SVD compression, one has

$$C_j^{\prime,\sigma_j} = U_j^{\prime,\sigma_j} S'_j V_j^{\prime,\dagger}. \tag{A4}$$

As in conventional DMRG, one can also introduce different weights in the direct sum and perform a SVD of the weighted sum of the reduced density matrix $\rho' = \sum_{k=0}^{3} w_k\rho_k$ Once this procedure is performed at site j, one can proceed updating all the tensors at site $j+1$. In formulas,

$$C'_{j+1} = \begin{pmatrix} C_{j+1}^{\sigma_{j+1}}[\psi]\\ C_{j+1}^{\sigma_{j+1}}[\phi]\\ C_{j+1}^{\sigma_{j+1}}[X^{\mathrm{Re}}]\\ C_{j+1}^{\sigma_{j+1}}[X^{\mathrm{Im}}]\end{pmatrix} = \begin{pmatrix} U_j^{[\prime,\dagger,\sigma_j]} C_j^{\sigma_j}[\psi] B_{j+1}^{\sigma_{j+1}}[\psi]\\ U_j^{[\prime,\dagger,\sigma_j]} C_j^{\sigma_j}[\phi] B_{j+1}^{\sigma_{j+1}}[\phi]\\ U_j^{[\prime,\dagger,\sigma_j]} C_j^{\sigma_j}[X^{\mathrm{Re}}] B_{j+1}^{\sigma_{j+1}}[X^{\mathrm{Re}}]\\ U_j^{[\prime,\dagger,\sigma_j]} C_j^{\sigma_j}[X^{\mathrm{Im}}] B_{j+1}^{\sigma_{j+1}}[X^{\mathrm{Im}}]\end{pmatrix}, \tag{A5}$$

where $U_j^{[\ell,\dagger,\sigma_j]}$ from Eq. (A4) is common to all the four vectors. After sweeping back and forth through the lattice, a *good* representation of the correction vectors is obtained.

[1] A. Damascelli, Z. Hussain, and Z.-X. Shen, Rev. Mod. Phys. **75**, 473 (2003).

[2] L. J. P. Ament, M. van Veenendaal, T. P. Devereaux, J. P. Hill, and J. van den Brink, Rev. Mod. Phys. **83**, 705 (2011).

[3] A. Nocera, U. Kumar, N. Kaushal, G. Alvarez, E. Dagotto, and S. Johnston, Sci. Rep. **8**, 11080 (2018).

[4] S. R. White, Phys. Rev. Lett. **69**, 2863 (1992).

[5] S. R. White, Phys. Rev. B **48**, 10345 (1993).

[6] U. Schollwöck, Ann. Phys. (Amsterdam) **326**, 96 (2011).

[7] S. R. White and A. E. Feiguin, Phys. Rev. Lett. **93**, 076401 (2004).

[8] A. J. Daley, C. Kollath, U. Schollwöck, and G. Vidal, J. Stat. Mech.: Theory Exp. (2004) P04005.

[9] S. R. White and I. Affleck, Phys. Rev. B **77**, 134437 (2008).

[10] M. Binder and T. Barthel, Phys. Rev. B **98**, 235114 (2018).

[11] S. Paeckel, T. Köhler, A. Swoboda, S. R. Manmana, U. Schollwöck, and C. Hubig, Ann. Phys. (Amsterdam) **411**, 167998 (2019).

[12] Y. Tian and S. R. White, Phys. Rev. B **103**, 125142 (2021).

[13] K. A. Hallberg, Phys. Rev. B **52**, R9827(R) (1995).

[14] P. E. Dargel, A. Honecker, R. Peters, R. M. Noack, and T. Pruschke, Phys. Rev. B **83**, 161104(R) (2011).

[15] P. E. Dargel, A. Wöllert, A. Honecker, I. P. McCulloch, U. Schollwöck, and T. Pruschke, Phys. Rev. B **85**, 205119 (2012).

[16] T. D. Kühner and S. R. White, Phys. Rev. B **60**, 335 (1999).

[17] S. K. Pati, S. Ramasesha, and D. Sen, Phys. Rev. B **55**, 8894 (1997).

[18] E. Jeckelmann, Phys. Rev. B **66**, 045114 (2002).

[19] E. Jeckelmann, Prog. Theor. Phys. Suppl. **176**, 143 (2008).

[20] A. Weichselbaum, F. Verstraete, U. Schollwöck, J. I. Cirac, and J. von Delft, Phys. Rev. B **80**, 165117 (2009).

[21] A. Nocera and G. Alvarez, Phys. Rev. E **94**, 053308 (2016).

[22] A. Holzner, A. Weichselbaum, I. P. McCulloch, U. Schollwöck, and J. von Delft, Phys. Rev. B **83**, 195115 (2011).

[23] F. A. Wolf, J. A. Justiniano, I. P. McCulloch, and U. Schollwöck, Phys. Rev. B **91**, 115144 (2015).

[24] J. C. Halimeh, F. Kolley, and I. P. McCulloch, Phys. Rev. B **92**, 115130 (2015).

[25] H. D. Xie, R. Z. Huang, X. J. Han, X. Yan, H. H. Zhao, Z. Y. Xie, H. J. Liao, and T. Xiang, Phys. Rev. B **97**, 075111 (2018).

[26] A. E. Feiguin and S. R. White, Phys. Rev. B **72**, 020404(R) (2005).

[27] See Supplemental Material at http://link.aps.org/supplemental/10.1103/PhysRevB.106.205106 for contains computational details and input files for the DMRG simulations, which includes Refs. [28,29].

[28] A. Scheie, P. Laurell, A. M. Samarakoon, B. Lake, S. E. Nagler, G. E. Granroth, S. Okamoto, G. Alvarez, and D. A. Tennant, Phys. Rev. B **103**, 224434 (2021).

[29] G. Alvarez, Comput. Phys. Commun. **180**, 1572 (2009).

[30] A. Nocera, N. D. Patel, J. Fernandez-Baca, E. Dagotto, and G. Alvarez, Phys. Rev. B **94**, 205145 (2016).

[31] A. Nocera, N. D. Patel, E. Dagotto, and G. Alvarez, Phys. Rev. B **96**, 205120 (2017).

[32] A. Nocera, Y. Wang, N. D. Patel, G. Alvarez, T. A. Maier, E. Dagotto, and S. Johnston, Phys. Rev. B **97**, 195156 (2018).

[33] U. Kumar, A. Nocera, E. Dagotto, and S. Johnston, Phys. Rev. B **99**, 205130 (2019).

[34] Y. Tseng, J. Thomas, W. Zhang, E. Paris, P. Puphal, R. Bag, G. Deng, T. C. Asmara, V. N. Strocov, S. Singh, E. Pomjakushina, U. Kumar, A. Nocera, H. M. Rønnow, S. Johnston, and T. Schmitt, npj Quantum Materials **7**, 92 (2022).

[35] J. Schlappa, T. Schmitt, F. Vernay, V. N. Strocov, V. Ilakovac, B. Thielemann, H. M. Rønnow, S. Vanishri, A. Piazzalunga, X. Wang *et al.*, Phys. Rev. Lett. **103**, 047401 (2009).

[36] S. Notbohm, P. Ribeiro, B. Lake, D. A. Tennant, K. P. Schmidt, G. S. Uhrig, C. Hess, R. Klingeler, G. Behr, B. Büchner *et al.*, Phys. Rev. Lett. **98**, 027403 (2007).

[37] M. Yang and S. R. White, Phys. Rev. B **102**, 094315 (2020).